ARL

US Army Research Laboratory

Tunable Solid-State Quantum Memory Using Rare-Earth-Ion-Doped Crystal, Nd³⁺:GaN

by S Rudin, BC Connelly, VS Malinovsky, RW Enck, and GD Metcalfe

NOTICES

Disclaimers

The findings in this report are not to be construed as an official Department of the Army position unless so designated by other authorized documents.

Citation of manufacturer's or trade names does not constitute an official endorsement or approval of the use thereof.

Destroy this report when it is no longer needed. Do not return it to the originator.

US Army Research Laboratory

Tunable Solid-State Quantum Memory Using Rare-Earth-Ion-Doped Crystal, Nd^{3+}:GaN

by S Rudin, BC Connelly, VS Malinovsky, RW Enck, and GD Metcalfe
Sensors and Electron Devices Directorate, ARL

REPORT DOCUMENTATION PAGE			*Form Approved* *OMB No. 0704-0188*	

Public reporting burden for this collection of information is estimated to average 1 hour per response, including the time for reviewing instructions, searching existing data sources, gathering and maintaining the data needed, and completing and reviewing the collection information. Send comments regarding this burden estimate or any other aspect of this collection of information, including suggestions for reducing the burden, to Department of Defense, Washington Headquarters Services, Directorate for Information Operations and Reports (0704-0188), 1215 Jefferson Davis Highway, Suite 1204, Arlington, VA 22202-4302. Respondents should be aware that notwithstanding any other provision of law, no person shall be subject to any penalty for failing to comply with a collection of information if it does not display a currently valid OMB control number.
PLEASE DO NOT RETURN YOUR FORM TO THE ABOVE ADDRESS.

1. REPORT DATE *(DD-MM-YYYY)*	2. REPORT TYPE	3. DATES COVERED (From - To)
April 2017	DRI Report	October 2014–October 2016

4. TITLE AND SUBTITLE	5a. CONTRACT NUMBER
Tunable Solid-State Quantum Memory Using Rare-Earth-Ion-Doped Crystal, Nd^{3+}:GaN	
	5b. GRANT NUMBER
	5c. PROGRAM ELEMENT NUMBER

6. AUTHOR(S)	5d. PROJECT NUMBER
S Rudin, BC Connelly, VS Malinovsky, RW Enck, and GD Metcalfe	DRI14-SE-002
	5e. TASK NUMBER
	5f. WORK UNIT NUMBER

7. PERFORMING ORGANIZATION NAME(S) AND ADDRESS(ES)	8. PERFORMING ORGANIZATION REPORT NUMBER
US Army Research Laboratory ATTN: RDRL-SEE-I 2800 Powder Mill Road Adelphi, MD 20783-1138	ARL-TR-8009

9. SPONSORING/MONITORING AGENCY NAME(S) AND ADDRESS(ES)	10. SPONSOR/MONITOR'S ACRONYM(S)
	11. SPONSOR/MONITOR'S REPORT NUMBER(S)

12. DISTRIBUTION/AVAILABILITY STATEMENT
Approved for public release; distribution unlimited.

13. SUPPLEMENTARY NOTES

14. ABSTRACT
The research objective of this Director's Research Initiative was to work on developing solid-state quantum memory using cryogenically cooled rare-earth-ion-doped crystal, Nd^{3+}:GaN. The samples were grown using the US Army Research Laboratory's molecular beam epitaxy (MBE) capabilities. The approach is based on the coherent transient interaction between light and the ions in a semiconductor. We investigated the energy level structure of the neodymium (Nd) ions embedded into the semiconductor crystal lattice, gallium nitride (GaN), and developed a quantum description of the 2- and 3-pulse photon echo effect. Epitaxial GaN:Nd was grown by plasma-assisted molecular beam epitaxy in a modular Gen II reactor using liquid gallium, solid Nd, and a nitrogen plasma. The photoluminescence (PL) spectrum from the lowest $^4F_{3/2}$ multiplet to all $^4I_{9/2}$ multiplets was measured by a free-space variable amplifier silicon diode. A demonstration of the coherence properties requires a high-quality sample with a narrow homogeneous broadening. For this reason, the PL linewidth was characterized for various growth conditions. The experiments were carried out to observe coherent effects, and various experimental setups are described. In parallel with experiments on the coherence properties of Nd^{3+}:GaN, we also investigated the effect of a varying electric field on the Nd PL spectrum to provide a tunable memory. To vary the applied field, we designed and grew a series of Nd-doped GaN *p-i-n* structures, strain-balanced superlattice structures, and periodic unbalanced structures.

15. SUBJECT TERMS
solid-state quantum memory, neodymium, 2-level system, Stark shift, heterostructure

16. SECURITY CLASSIFICATION OF:			17. LIMITATION OF ABSTRACT	18. NUMBER OF PAGES	19a. NAME OF RESPONSIBLE PERSON
			UU	44	S Rudin
a. REPORT	b. ABSTRACT	c. THIS PAGE			19b. TELEPHONE NUMBER (Include area code)
Unclassified	Unclassified	Unclassified			301-394-0206

Standard Form 298 (Rev. 8/98)
Prescribed by ANSI Std. Z39.18

Contents

List of Figures

1.   Summary

The research objective of this Director's Research Initiative was to work on developing solid-state quantum memory using cryogenically cooled rare-earth-ion-doped crystal, Nd^{3+}:GaN. The samples were grown using the US Army Research Laboratory's molecular beam epitaxy (MBE) capabilities. The approach is based on the coherent transient interaction between light and the ions in a semiconductor. We investigated the energy level structure of the neodymium (Nd) ions embedded into the semiconductor crystal lattice, gallium nitride (GaN), and developed a quantum description of the 2- and 3-pulse photon echo effect. Epitaxial GaN:Nd was grown by plasma-assisted MBE in a modular Gen II reactor using liquid gallium, solid Nd, and a nitrogen plasma. The photoluminescence (PL) spectrum from the lowest $^4F_{3/2}$ multiplet to all $^4I_{9/2}$ multiplets was measured by a free-space variable amplifier silicon diode. A demonstration of the coherence properties requires a high-quality sample with a narrow homogeneous broadening. For this reason, the PL linewidth was characterized for various growth conditions. The experiments were carried out to observe coherent effects, and various experimental setups are described. In parallel with experiments on the coherence properties of Nd^{3+}:GaN, we also investigated the effect of a varying electric field on the Nd PL spectrum to provide a tunable memory. To vary the applied field, we designed and grew a series of Nd-doped GaN *p-i-n* structures, strain-balanced superlattice structures, and periodic unbalanced structures.

2.   Introduction

Because of an increasing demand to process large databases in real time, the Army has a clear interest in realizing quantum computing. The Army also has a great interest in new approaches to secure communications. This can be answered by quantum communication schemes using polarization states of photons. Realization of quantum information and quantum communication, which promise unprecedented computational capacities via quantum computing and unconditional communication security via quantum cryptography, stimulated some new approaches to optical storage.[1] Quantum information processing requires temporal storage for quantum data. The coherent, efficient, and reversible mapping between quantum light and matter represents a fundamental challenge in the field of quantum information science. Overcoming this challenge would enable the realization of a quantum memory for light, a device that can store and, on-demand, recall quantum states of light with high efficiency and fidelity. Such memories have potential applications for use in a quantum repeater, a resource allowing for quantum communication over long distances. Other applications include linear

1

optics quantum computation, deterministic single photon sources and multiphoton quantum-state engineering. For practical applications, it is likely that a quantum memory with a high multimode capacity will be necessary.

The research objective of this Director's Research Initiative (DRI) was to work on developing solid-state quantum memory using cryogenically cooled rare-earth-ion-doped crystal, Nd^{3+}:GaN. The samples were grown using the US Army Research Laboratory's (ARL's) molecular beam epitaxy (MBE) capabilities. The approach is based on the coherent transient interaction between light and the ions in a semiconductor. We investigated the energy level structure of the neodymium (Nd) ions embedded into the semiconductor crystal lattice, gallium nitride (GaN), and developed a quantum description of the 2- and 3-pulse photon echo effect. To do so, we identified the range of photon frequencies that can be efficiently stored in the quantum memory. Applied electric field gradients are required for controlled inhomogeneous broadening. This was accomplished using semiconductor p-n junctions and GaN/AlGaN heterostructures, which allow us to apply much stronger fields than currently possible in quantum memories based on insulating crystals and glasses. In addition, the strong internal electric fields in GaN polar heterostructures provide a unique opportunity to control the frequency of the electronic transitions and design a quantum memory with a multimode capacity. Also, the use of semiconducting host materials may allow optical control of the relevant electronic transitions and field control through screening in the future designs of quantum memories.

3.   Approach to Achieving Research Objectives

Many different approaches toward developing quantum memory have been proposed. Recently, significant progress has been achieved using atomic ensembles for manipulating the propagation and quantum state of an optical field.[2] The rare-earth-ion-doped crystals (REICs) are promising candidates for quantum memory. REICs are characterized by large optical inhomogeneous broadening that enables storage and recall of coherent information by manipulating and controlling the inhomogeneous dephasing using echo techniques. Although traditional photon echoes are not directly used in the single-photon regime because of spontaneous emission noise induced by the π-pulse,[3] photon echo techniques avoiding this noise have been proposed: controlled reversible inhomogeneous broadening (CRIB)[4] and more recently atomic frequency combs (AFCs).[5]

3.1 Quantum Memory Based on 2-Pulse Photon Echo

As we mentioned previously, the traditional photon-echo-based memory generally suffers from strong limitations when used for storage of single photons; therefore, it cannot be directly used for quantum communication.[6] However, the standard photon echo studies are a critical first step and give rise to the development of the quantum storage approach based on CRIB, which is well suited for storage of single photons. We therefore give a brief description of the traditional 2-pulse photon echo technique.

The underlying principle of quantum memory based on the photon echo technique can readily be explained in a Bloch vector representation since it allows for a geometrical interpretation of the density matrix evolution. Using Pauli matrix decomposition, one can map the evolution of the 2-level system (representing selected states of the rare-earth ion in the solids) into rotation of the 3-D Bloch vector $\mathbf{B} = (u, v, w) = (\rho_{12} + \rho_{21}, i(\rho_{21} - \rho_{12}), \rho_{22} - \rho_{11})$, where $\rho_{11,22}$ is the population of the states, and ρ_{12} is the coherence. Figure 1 shows a schematic of the 2-pulse photon echo in the Bloch vector representation.
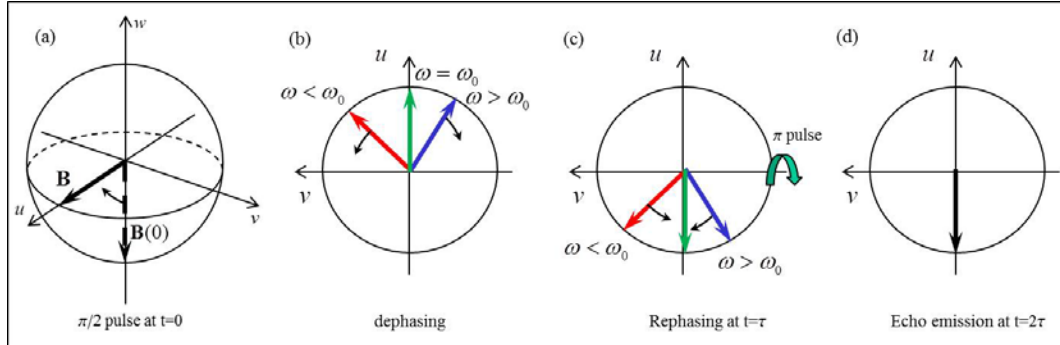
Fig. 1 **Evolution of the Bloch vector during the 2-pulse photon-echo process. a) $\pi/2$ pulse rotates the Bloch vector from the negative w axis along the u direction. b) The individual Bloch vectors precess in the uv plane and dephase due to the inhomogeneous broadening of the transition. c) At time $t = \tau$, a π-pulse rotates all Bloch vectors around the v axis. d) The Bloch vectors realign and build up a macroscopic coherence that results in a photon-echo emission at time $t = 2\tau$.**

In some cases, analytic calculations of the echo signal intensity can be carried out using coupled Maxwell-Bloch equations.[7] Taking into account the inhomogeneous distribution of the transition frequency, one can find the intensity of the echo signal $P(t) \propto \sin\left(A_1\right) \sin^4\left(A_2/2\right) e^{-2\gamma t} e^{-\sigma^2(t-2\tau)^2/2}$, where A_k is the pulse area of the k-pulse, $k = 1,2$, γ is the dephasing rate, and σ is the width of the inhomogeneous distribution. The dimensionless pulse area is defined as a time integral over the electric field amplitude $E_0(t)$ multiplied by the electric dipole moment of the interlevel transition

d$_{12}$ and divided by Plank's constant. It is not necessary that the pulse areas be equal to $\pi/2$ and π, although these areas lead to a maximal signal. What *is* necessary is that the second pulse produces at least a partial reflection about the *uw* plane. This reflection takes the Bloch vector components $u + iv$ into $u - iv$ or, equivalently, takes density matrix element ρ_{12} into ρ_{21}. Since ρ_{12} and ρ_{21} are related to the real and imaginary parts of the average dipole moment operator, the second pulse must couple these real and imaginary parts. Such coupling is impossible for a linear atom–field interaction. Thus, by its very nature, the photon echo can occur only when a nonlinear atomic response is present.

3.2 Quantum Memory Based on Controlled Reversible Inhomogeneous Broadening (CRIB)

A few decades ago, researchers demonstrated how to benefit from the large ratio between the homogeneous and inhomogeneous linewidths.[8] The CRIB photon-echo technique is a 4-wave mixing technique, with pulses being separated in time. The 3 input pulses manipulate the system, putting the absorbers in the material in superposition states, which at some given time all oscillate in phase creating a macroscopic dipole moment. The output pulse (*echo*) is emitted by this temporally created macroscopic dipole moment. To store a sequence of data, a short preparation (write) pulse, $E_w(t)$, with a pulse area equal to $\pi/2$ and a bandwidth equal or larger than the required data rate is sent into the sample (Fig. 2). The data pulse sequence, $E_d(t)$, at a maximum data rate equal to the bandwidth of the pulse $E_w(t)$, and duration shorter than the homogeneous relaxation time of the absorbers, is then sent into the media. The input radiation (both write and data pulses) interacts coherently with the absorbers. As a result, the frequency spectrum of the input data sequence (amplitude as well as phase) becomes imprinted as a frequency-dependent modulation onto the absorption profile. Since both amplitude and phase are stored, the full temporal information of the light pulses is contained in the spectral interference patterns engraved in the sample, and later pulses can interact with these spectral gratings to perform read-out. Mathematically, it can be expressed by the following Fourier transform equation. When the electromagnetic fields of the 3 input pulse sequences, $E_w(t)$, $E_d(t)$, and $E_r(t)$, are far from saturating the optical transition and the time separation between the pulse sequences is smaller than the transition relaxation time, the output field, $E_e(t)$, as a function of time is $E_e(t) \propto \int E_w^*(\omega) E_d(\omega) E_r(\omega) e^{i\omega t} d\omega$. It is clear that the echo field is just a copy of the $E_d(t)$ when the spectra of $E_w(\omega)$ and $E_r(\omega)$ are constant across the data bandwidth, $E_d(\omega)$.
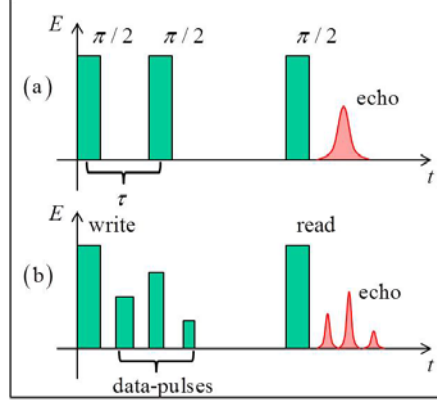
Fig. 2 **a) Stimulated photon-echo schematic. b) Generalization of the 3-pulse echo to data storage.**

The CRIB approach involves broadening an initially narrow absorption line using the linear Stark effect and an applied external electric field gradient.[9] The width of the broadened line should match the spectral width of the light that is to be absorbed. Read out or re-emission of the stored light is triggered by changing the sign of the external electric field, which inverts the atomic transition frequencies around the central frequency. The rephasing mechanism can be understood by the following argument. Atoms at detuning Δ with respect to the carrier frequency of the light accumulate a phase $-i\Delta\tau$ between absorption at $t = 0$ and the polarity inversion of the electric field at $t = \tau$. By inverting the polarity, the atoms invert their detunings $\Delta \rightarrow -\Delta$. After a time $t = 2\tau$ the atoms will have accumulated an opposite phase factor $i\Delta\tau$ that results in a rephasing of all atomic dipoles.[1] A schematic of the CRIB protocol is shown in Fig. 3.
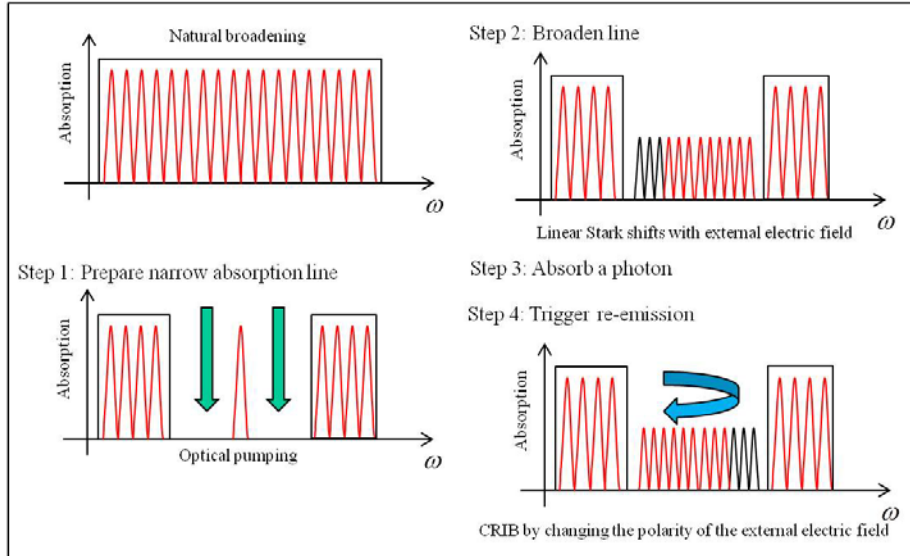
Fig. 3 **Quantum state storage based on CRIB in crystals with an ensemble of ions having a broad, inhomogeneously broadened absorption line**

4.   Electronic States in Rare Earth Ions

In this study we use Nd^{3+}:GaN.[10] Rare-earth-ion-doped solids are of particular interest because of the absence of motion of the absorbers, as well as their excellent optical and hyperfine coherence times at cryogenic temperatures, which promise long storage times. As a result of different strains in the host medium, they also exhibit large inhomogeneous broadening on their optical transitions, which provides the fast decay of excited atomic coherence upon absorption of broadband light. The ratio between the inhomogeneous and homogeneous transition linewidths can get up to 10^8 in REICs.[11] Therefore, by using the frequency dimension to address and store optical data, one could potentially store and address thousands of data bits at a single spatial location.

Material requirements for CRIB-based quantum memory include the possibility to inhomogeneously broaden an optical transition in a controlled way. The induced broadening needs to be large compared to the inherent broadening of the transition, and it should be possible to reverse it in a short amount of time compared to the inverse of the inherent broadening. The shielding of the $4f$ electrons reduces electron orbit–lattice interaction as compared to other solids, thereby minimizing the effect of dynamic perturbations by phonons. This results in a transition intensity concentrated in narrow zero-phonon lines. For crystalline hosts the homogeneous linewidths are typically around a few kilohertz.[1]

The ion energy levels can be manipulated using the Zeeman and Stark effects. Of particular interest for CRIB is the linear Stark effect. For an impurity ion in an inversionless crystal field, the states of different parity are mixed and thus a linear Stark effect in an external electric field is possible.[12] Provided the permanent electric dipole moments of the states coupled by the optical field are different, it leads to a shift in resonance frequency, which can be exploited for controlled reversible inhomogeneous broadening of the associated transition. The magnitude of the Stark shift depends on the particular transition, the crystal host, and the orientation of the electric field with respect to the permanent dipole moment difference. The largest Stark shifts are of the order of 100 kHz/Vcm^{-1}.[12] In RE-doped crystals, where the application of a DC electric field leads to a shift or discrete splitting of an absorption line, controlled inhomogeneous broadening on the order of several hundred megahertz can potentially be induced by applying an electric field gradient with a field strength varying between –1000 Vcm^{-1} and +1000 Vcm^{-1}.

Nd^{3+} has three $4f$ electrons (14 electrons are needed to completely fill the shell). Labeling the various levels is based on the Russell-Saunders (RS) coupling scheme. In the RS scheme the interaction between orbital and spin angular momenta of the electrons is neglected in the first approximation, and the total orbital angular momentum is quantized.

The orbital-momentum vectors of 2 electrons l_1 and l_2 give the total momentum L with values from l_1+L_2 to $|l_1-l_2|$. The $4f$ electron has $l = 3$. Each value of L is similarly coupled to l_3, and so on. The total orbital momenta $L = 0,1,2,3,4,5,6,7,8,9,10,11$ corresponds to electronic terms $S,P,D,F,G,H,I,K,L,M,N,O,Q$. Similarly, the spin momenta of the individual $4f$ electrons are vectorially added to give S.

5.   Review of Previous Growth of Neodymium (Nd)-Doped Gallium Nitride (GaN)

Nd has previously been incorporated into GaN through ion implantation and reactive cosputtering deposition. Ion implantation has limitations due to damage effects and doping profiles. In many cases, a postimplantation anneal is required because of the amorphization of the GaN lattice; however, annealing does not completely recover the damage. For ion-implanted Nd in GaN, the majority of Nd^{3+} ions sit on the Ga substitutional "site"; however, 4 other sites associated with impurities and defects are also identified within the GaN matrix. For reactive cosputtering deposition of GaN with RE atoms, a postgrowth anneal ($\geq$700 °C) in nitrogen is also necessary for photoluminescence (PL) emission. As part of previous DRI work at ARL, we successfully achieved in situ Nd doping of high crystal quality GaN grown by plasma-assisted MBE.[13] The GaN:Nd samples, without any postgrowth annealing, exhibited strong PL emission under direct pumping of the Nd centers that could be identified with the $^4F_{3/2} \rightarrow ^4I_{9/2}$, $^4F_{3/2} \rightarrow ^4I_{11/2}$, and $^4F_{3/2} \rightarrow ^4I_{13/2}$ multiplets (Fig. 4). Moreover, the scarcity and relative weakness of the emission from extra PL peaks from above bandgap pumping suggest improved incorporation at the Ga substitutional sites and allowed us to resolve the Stark energy sublevels of the $4f$ states using PL and photoluminescence excitation (PLE) spectroscopies.[10]
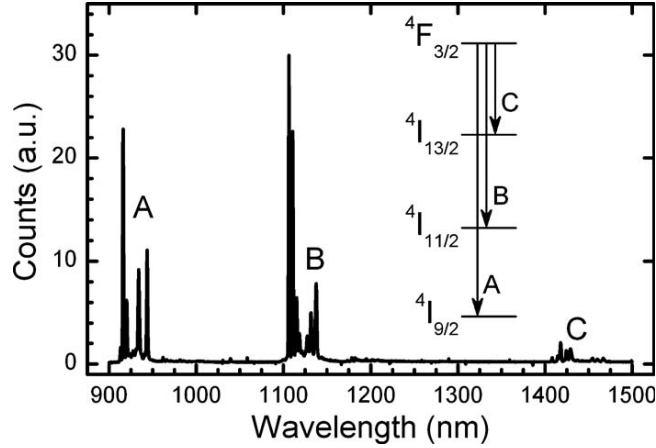
Fig. 4 Low-temperature (~30 K) PL from 900 to 1500 nm for GaN:Nd pumped at 836 nm showing the characteristic Nd transitions. (Reprinted from Readinger et al.[13])

The GaN layers were grown on single-side polished *c*-plane sapphire by MBE using standard effusion cells and a UNI-Bulb RF plasma source for activated nitrogen. Following the sapphire nitridation, an aluminum nitride (AlN) buffer layer of approximately 25 nm was grown. The buffer was followed by a 200-nm undoped GaN base layer and a Nd-doped approximately 1-µm GaN layer with various Nd concentrations up to approximately 5 atomic-percent (at%). The Nd cell temperature was adjusted while maintaining fixed growth conditions (growth temperature, Ga flux, nitrogen flux, rf power, nitrogen gas flow rate, etc.) to control the dopant incorporation.

The material grown for this work was analyzed using Rutherford backscattering spectroscopy and secondary ion mass spectrometry (SIMS) for quantitative analysis of the Nd concentration, X-ray diffraction (XRD) for structural quality, and PL, PLE, reflectance, and transmittance.

6. Theoretical Analyses of 2- and 3-Level Models and Design Parameters

6.1 2-Level System

In the rotating wave approximation (RWA), the Hamiltonian has the form

$$H = -\frac{\hbar}{2}\begin{pmatrix} 0 & \Omega \\ \Omega & 2\Delta\omega \end{pmatrix},\tag{1}$$

where $\Delta\omega = \omega - E_2/\hbar$ is the detuning between the transition frequency and the center frequency of the laser field, taken as $E(t) = E_0(t)\cos(\omega t + \phi_0)$, $\Omega = E_0(t)d_{12}/\hbar$ is the Rabi frequency, d_{12} is the dipole moment. The model is illustrated in Fig. 5.
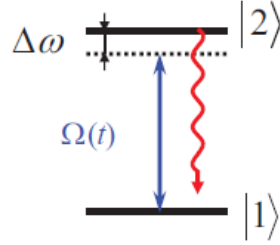
Fig. 5 **Schematic of a 2-level system**

To take into account spontaneous decay of the exited state, it is constructive to rewrite the density matrix equation ($\dot{\rho}(t) = -i/\hbar[H\rho - \rho H]$) in the Liouvillian form

$$\dot{X}(t) = -(L_d + L_r)X(t), \tag{2}$$

where

$$X(t) = \begin{pmatrix} \rho_{12}(t) \\ \rho_{21}(t) \\ \rho_{11}(t) \\ \rho_{22}(t) \end{pmatrix}, \tag{3}$$

the dynamical part of the Liouvillian is

$$L_d = \begin{pmatrix} i\Delta\omega & 0 & \dfrac{i\Omega}{2} & -\dfrac{i\Omega}{2} \\ 0 & -i\Delta\omega & -\dfrac{i\Omega}{2} & \dfrac{i\Omega}{2} \\ \dfrac{i\Omega}{2} & -\dfrac{i\Omega}{2} & 0 & 0 \\ -\dfrac{i\Omega}{2} & \dfrac{i\Omega}{2} & 0 & 0 \end{pmatrix}, \tag{4}$$

the relaxation and dephasing are taken into account by using the superoperator

$$L_r = \begin{pmatrix} \dfrac{1}{T_2^*} & 0 & 0 & 0 \\ 0 & \dfrac{1}{T_2^*} & 0 & 0 \\ 0 & 0 & 0 & -\dfrac{1}{T_1} \\ 0 & 0 & 0 & \dfrac{1}{T_1} \end{pmatrix}, \tag{5}$$

$1/T_2^* = 1/(2T_1) + \Gamma$ is the dephasing rate, and T_1 is the life time of the excited state.

The exact form of the dynamic equation for the density matrix elements is

$$\begin{aligned}
\dot{\rho}_{12} &= \rho_{12}(-i\Delta\omega - 1/T_2^*) - (\rho_{11} - \rho_{22})i\Omega/2, \\
\dot{\rho}_{21} &= \rho_{21}(i\Delta\omega - 1/T_2^*) + (\rho_{11} - \rho_{22})i\Omega/2, \\
\dot{\rho}_{11} &= \rho_{22}/T_1 + (\rho_{21} - \rho_{12})i\Omega/2, \\
\dot{\rho}_{22} &= -\rho_{22}/T_1 - (\rho_{21} - \rho_{12})i\Omega/2.
\end{aligned} \tag{6}$$

Taking into account that $\rho_{11}(t) + \rho_{22}(t) = 1$, we find the steady-state solution

$$\begin{aligned}
\rho_{12}^s &= \frac{\Omega}{2} \frac{\Delta\omega - 1/T_2^*}{\Delta\omega^2 + 1/T_2^{*2} + \Omega^2 T_1/T_2^*}, \\
\rho_{12}^s &= \frac{\Omega}{2} \frac{\Delta\omega + 1/T_2^*}{\Delta\omega^2 + 1/T_2^{*2} + \Omega^2 T_1/T_2^*}, \\
\rho_{11}^s &= 1 - \frac{1}{2} \frac{\Omega^2 T_1/T_2^*}{\Delta\omega^2 + 1/T_2^{*2} + \Omega^2 T_1/T_2^*}, \\
\rho_{22}^s &= \frac{1}{2} \frac{\Omega^2 T_1/T_2^*}{\Delta\omega^2 + 1/T_2^{*2} + \Omega^2 T_1/T_2^*}.
\end{aligned} \tag{7}$$

We see that in the resonant case, $\Delta\omega = 0$, the population of the excited state is

$$\rho_{22}^s = \frac{1}{2} \frac{\Omega^2 T_1 T_2^*}{1 + \Omega^2 T_1 T_2^*}, \tag{8}$$

and in the limit $\Omega^2 T_1 T_2^* \gg 1$ the state populations of the 2-level system $\rho_{11}^s = \rho_{22}^s = 1/2$.

6.2 Bloch Equations

Using $\rho_{12} = \rho_{21}^* = (u - iv)/2$, $\quad \rho_{22} - \rho_{11} = n$, and $\rho_{22} + \rho_{11} = 1$, we can rewrite the density matrix (Eq. 6) in the Bloch equation form as

$$\dot{u} = -u/T_2^* + \Delta\omega v,$$
$$\dot{v} = -v/T_2^* - \Delta\omega u - \Omega n, \qquad (9)$$
$$\dot{n} = (n+1)/T_1 + \Omega v.$$

6.3 3-Level System and Fast Nonradiative Decay of the Top Level

To describe fluorescence from an additional level |3> populated by fast nonradiative transition from the excited state |2>, we consider the 3-level system shown in Fig. 6.
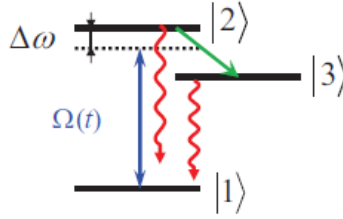
Fig. 6   **Schematic of a 3-level system with nonradiative decay of the top level**

In this case, we have to include an additional equation of motion of the population of the excited state |3>. The dynamical part of the Liouvillian, Eq. 4, does not change while the relaxation part, Eq. 5, becomes

$$L_r = \begin{pmatrix} 1/T_2^* + \gamma_n/2 & 0 & 0 & 0 & 0 \\ 0 & 1/T_2^* + \gamma_n/2 & 0 & 0 & 0 \\ 0 & 0 & 0 & -1/T_1 & -1/T_1^{(3)} \\ 0 & 0 & 0 & 1/T_1 + \gamma_n & 0 \\ 0 & 0 & 0 & -\gamma_n & 1/T_1^{(3)} \end{pmatrix}, \qquad (10)$$

where γ_n is the nonradiative decay rate of the state |2>, and $T_1^{(3)}$ is the lifetime of the state |3>.

The system of the dynamic equation for the density matrix elements becomes

$$\dot{\rho}_{12} = \rho_{12}(-i\Delta\omega - 1/T_2^* - \gamma_n/2) - (\rho_{11} - \rho_{22})i\Omega/2,$$

$$\dot{\rho}_{21} = \rho_{21}(i\Delta\omega - 1/T_2^* - \gamma_n/2) + (\rho_{11} - \rho_{22})i\Omega/2,$$

$$\dot{\rho}_{11} = \rho_{22}/T_1 + \rho_{33}/T_1^{(3)} + (\rho_{21} - \rho_{12})i\Omega/2, \qquad (11)$$

$$\dot{\rho}_{22} = -\rho_{22}(1/T_1 + \gamma_n) - (\rho_{21} - \rho_{12})i\Omega/2,$$

$$\dot{\rho}_{33} = \rho_{22}\gamma_n - \rho_{33}/T_1^{(3)}.$$

Taking into account that $\rho_{33} + \rho_{22} + \rho_{11} = 1$, we find the steady-state solution

$$\rho_{12}^s = -\frac{iT_2^*\Omega(\gamma_n T_1 + 1)(2 + T_2^*(\gamma_n + 2i\Delta\omega))}{\Omega^2 T_1 T_2^*(\gamma_n T_1^{(3)} + 2)(\gamma_n T_2^* + 2) + (\gamma_n T_1 + 1)(4\Delta\omega^2 T_2^{*2} + (\gamma_n T_2^* + 2)^2)},$$

$$\rho_{12}^s = \frac{T_2^*\Omega(\gamma_n T_1 + 1)(2i + T_2^*(i\gamma_n + 2\Delta\omega))}{\Omega^2 T_1 T_2^*(\gamma_n T_1^{(3)} + 2)(\gamma_n T_2^* + 2) + (\gamma_n T_1 + 1)(4\Delta\omega^2 T_2^{*2} + (\gamma_n T_2^* + 2)^2)},$$

$$\rho_{11}^s = \frac{(\gamma_n T_1 + 1)(4\Delta\omega^2 T_2^{*2} + (\gamma_n T_2^* + 2)^2) + \Omega^2 T_1 T_2^*(\gamma_n T_2^* + 2)}{\Omega^2 T_1 T_2^*(\gamma_n T_1^{(3)} + 2)(\gamma_n T_2^* + 2) + (\gamma_n T_1 + 1)(4\Delta\omega^2 T_2^{*2} + (\gamma_n T_2^* + 2)^2)}, \qquad (12)$$

$$\rho_{22}^s = \frac{\Omega^2 T_1 T_2^*(\gamma_n T_2^* + 2)}{\Omega^2 T_1 T_2^*(\gamma_n T_1^{(3)} + 2)(\gamma_n T_2^* + 2) + (\gamma_n T_1 + 1)(4\Delta\omega^2 T_2^{*2} + (\gamma_n T_2^* + 2)^2)},$$

$$\rho_{33}^s = \frac{\gamma_n T_1 T_2^* T_1^{(3)}\Omega^2(\gamma_n T_2^* + 2)}{\Omega^2 T_1 T_2^*(\gamma_n T_1^{(3)} + 2)(\gamma_n T_2^* + 2) + (\gamma_n T_1 + 1)(4\Delta\omega^2 T_2^{*2} + (\gamma_n T_2^* + 2)^2)}.$$

Note that Eq. 12 is identical to Eq. 7 in the limit $\gamma_n \to 0$.

In the steady-state regime, from the equation for ρ_{33}, Eq. 11, we see that $\rho_{33}^s = T_1^{(3)}\gamma_n\rho_{22}^s$. Therefore, now we consider steady-state expression for the ρ_{22}^s. For the resonant excitation, $\Delta\omega = 0$, we obtain

$$\rho_{22}^s = \frac{\Omega^2 T_1 T_2^*}{\Omega^2 T_1 T_2^*(\gamma_n T_1^{(3)} + 2) + (\gamma_n T_1 + 1)(\gamma_n T_2^* + 2)}. \qquad (13)$$

Assuming that $\gamma_n T_1 \gg 1$ and $T_1^{(3)} \approx T_1$, we find

$$\rho_{22}^s = \frac{1}{\gamma_n T_1^{(3)}}\frac{\Omega^2 T_1 T_2^*}{\Omega^2 T_1 T_2^* + T_1(\gamma_n T_2^* + 2)/T_1^{(3)}} = \frac{1}{\gamma_n T_1^{(3)}}\frac{\Omega^2 T_1^{(3)} T_2^*}{\Omega^2 T_2^* T_1^{(3)} + \gamma_n T_2^* + 2}. \qquad (14)$$

Therefore,

$$\rho_{33}^s \approx \frac{\Omega^2 T_1^{(3)} T_2^*}{\Omega^2 T_2^* T_1^{(3)} + \gamma_n T_2^* + 2}. \qquad (15)$$

6.4 3-Level System and Fast Nonradiative Decay of the Intermediate Level

Figure 7 shows a schematic of the 3-level system with fast nonradiative decay of the intermediate level |3>.
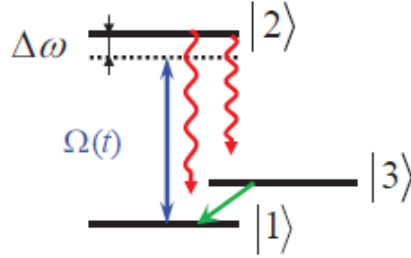
Fig. 7   **Schematic of a 3-level system with nonradiative decay of the intermediate level**

In this case, the dynamical part of the Liouvillian, Eq. 4, does not change while the relaxation part, Eq. 10, becomes

$$L_r = \begin{pmatrix} 1/T_2^* & 0 & 0 & 0 & 0 \\ 0 & 1/T_2^* & 0 & 0 & 0 \\ 0 & 0 & 0 & -1/T_1 & -\gamma_n \\ 0 & 0 & 0 & 1/T_1 + 1/T_{23} & 0 \\ 0 & 0 & 0 & -1/T_{23} & \gamma_n \end{pmatrix}, \tag{16}$$

where $1/T_{23}$ is the radiative decay rate of the state |2> to the state |3>, and γ_n is the nonradiative decay rate of the state |3>. Now $1/T_2^* = 1/2(1/T_1 + 1/T_{23}) + \Gamma$.

The system of the dynamic equation for the density matrix elements becomes

$$\begin{aligned}
\dot{\rho}_{12} &= \rho_{12}(i\Delta\omega - 1/T_2^*) - (\rho_{11} - \rho_{22})i\Omega/2, \\
\dot{\rho}_{21} &= \rho_{21}(-i\Delta\omega - 1/T_2^*) + (\rho_{11} - \rho_{22})i\Omega/2, \\
\dot{\rho}_{11} &= \rho_{22}/T_1 + \rho_{33}\gamma_n + (\rho_{21} - \rho_{12})i\Omega/2, \\
\dot{\rho}_{22} &= -\rho_{22}(1/T_1 + 1/T_{23}) - (\rho_{21} - \rho_{12})i\Omega/2, \\
\dot{\rho}_{33} &= \rho_{22}/T_{23} - \rho_{33}\gamma_n.
\end{aligned} \tag{17}$$

Again, taking into account that $\rho_{33} + \rho_{22} + \rho_{11} = 1,$ we find the steady-state solution

$$\rho_{12}^s = -\frac{iT_2^*\Omega(\gamma_n T_1 + 1)(2 + T_2^*(\gamma_n + 2i\Delta\omega))}{\Omega^2 T_1 T_2^*(\gamma_n T_1^{(3)} + 2)(\gamma_n T_2^* + 2) + (\gamma_n T_1 + 1)(4\Delta\omega^2 T_2^{*2} + (\gamma_n T_2^* + 2)^2)},$$

$$\rho_{12}^s = \frac{\gamma_n T_2^*\Omega(T_1 + T_{23})(T_2^*\Delta\omega - i)}{\Omega^2 T_1 T_2^*(\gamma_n T_1^{(3)} + 2)(\gamma_n T_2^* + 2) + (\gamma_n T_1 + 1)(4\Delta\omega^2 T_2^{*2} + (\gamma_n T_2^* + 2)^2)},$$

$$\rho_{11}^s = \frac{(\gamma_n T_1 + 1)(4\Delta\omega^2 T_2^{*2} + (\gamma_n T_2^* + 2)^2) + \Omega^2 T_1 T_2^*(\gamma_n T_2^* + 2)}{\Omega^2 T_1 T_2^*(\gamma_n T_1^{(3)} + 2)(\gamma_n T_2^* + 2) + (\gamma_n T_1 + 1)(4\Delta\omega^2 T_2^{*2} + (\gamma_n T_2^* + 2)^2)}, \qquad (18)$$

$$\rho_{22}^s = \frac{\Omega^2 T_1 T_2^*(\gamma_n T_2^* + 2)}{\Omega^2 T_1 T_2^*(\gamma_n T_1^{(3)} + 2)(\gamma_n T_2^* + 2) + (\gamma_n T_1 + 1)(4\Delta\omega^2 T_2^{*2} + (\gamma_n T_2^* + 2)^2)},$$

$$\rho_{33}^s = \frac{\gamma_n T_1 T_2^* T_1^{(3)}\Omega^2(\gamma_n T_2^* + 2)}{\Omega^2 T_1 T_2^*(\gamma_n T_1^{(3)} + 2)(\gamma_n T_2^* + 2) + (\gamma_n T_1 + 1)(4\Delta\omega^2 T_2^{*2} + (\gamma_n T_2^* + 2)^2)}.$$

In the steady-state regime, from the equation for ϱ_{33}, Eq. 17, we see that $\varrho_{22}^s = T_{23}\gamma_n\varrho_{33}^s$. Therefore, now we consider the steady-state expression for ϱ_{22}^s.

For the resonant excitation, $\Delta\omega = 0$, we obtain

$$\varrho_{22}^s = \frac{\gamma_n T_1 T_2^* T_{23}\Omega^2}{2\gamma_n(T_1 + T_{23}) + T_1 T_2^*\Omega^2(2\gamma_n T_{23} + 1)}. \qquad (19)$$

Assuming that $\gamma_n T_{23} \gg 1$, we obtain

$$\varrho_{22}^s = \frac{1}{2}\frac{T_1 T_2^*\Omega^2}{T_1/T_{23} + 1 + T_1 T_2^*\Omega^2}. \qquad (20)$$

The steady-state population of the excited level is very similar to the 2-level system case, Eq. 8, in the limit $\Omega_2 T_1 T_2^* \to \infty$ the state populations $\varrho_{11}^s = \varrho_{22}^s = 1/2$. The difference is that now we have population inversion on the $|2\rangle - |3\rangle$ transition, since $\varrho_{33}^s \to 0$; to be exact, it goes as $1/T_{23}\gamma_n$, which is much less than 1.

7. Steady-State Population

Figure 8 shows the steady-state population in Eq. 8 as a function of the Rabi frequency. As mentioned previously, the population of the states is equal to 1/2 at the limit $\Omega \sqrt{T_1 T_2^*} \to \infty$.

Introducing a new variable $x = \Omega\sqrt{T_1 T^*_2}$, we see that the steady-state population in Eq. 8 is $f(x) = 0.5x^2/(1+x^2)$. The second derivative (Fig. 9) of this function is equal to zero at $x_0 = 1/\sqrt{3}$ (therefore, $\Omega 0 = 1/\sqrt{3}T_1 T^*_2$), which can be used to determine the dipole moment from the experimental data. Figure 10 shows the steady-state population in Eq. 15 as function of the Rabi frequency. We assume that $T_1 \approx T^{(3)}_1$, $\Gamma T_1 \gg 1$, and $\gamma_n/\Gamma = 10$. For comparison, the dashed line shows the steady-state population in Eq. 8.

Fig. 8   Steady-state population in 2-level system, Eq. 8
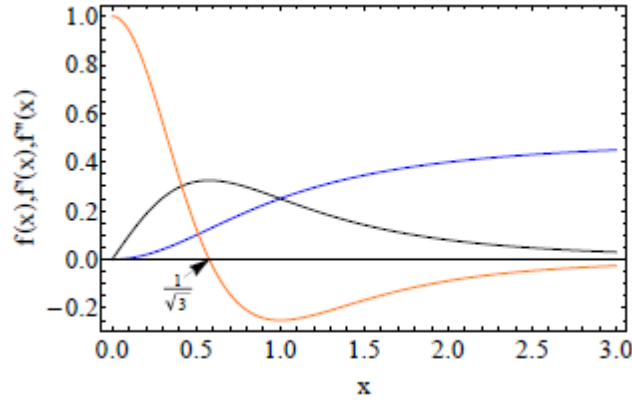
Fig. 9   Useful dependencies to analyze the steady-state population as a function of the field amplitude

$$\Omega\sqrt{T_1 T_2^*}$$

Fig. 10   Steady-state population, see Eqs. 8 and 15

Figure 11 shows $f(x) = x^2/(a^2 + x^2)$ ($a2 = \gamma_n T*_2 + 2$), its first and second derivatives as a function of $x = \Omega\sqrt{T^{(3)}_1} T*_2$. The second derivative of this function is equal to zero at $x_0 = a/\sqrt{3}$; therefore, $\Omega_0 = \sqrt{\gamma_n T*_2 + 2}/\sqrt{3}T_1 T*_2$.
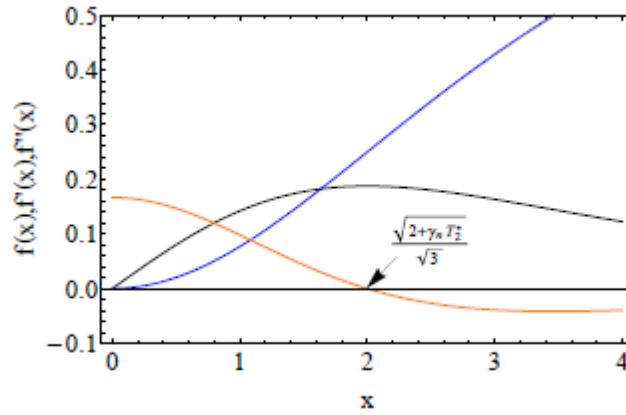
Fig. 11   Useful dependencies to analyze the steady-state population as a function of the field amplitude

Figure 12 shows the steady-state population in Eq. 20 as a function of the Rabi frequency.

We assume that $T_1 \approx T_{23}$, and $\gamma_n T_{23} \gg 1$. For comparison, the dashed line shows the steady-state population in Eq. 8. Figure 13 shows $f(x) = 0.5x^2/(a^2+x^2)$ ($a^2 = T_1/T_{23}+1$), its first and second derivatives as a function of $x = \Omega\sqrt{T_1 T*_2}$. The second derivative of this function is equal to zero at $x_0 = a/\sqrt{3}$; therefore, $\Omega_0 = \sqrt{T_1/T_{23} + 1}/\sqrt{3}T_1 T*_2$.
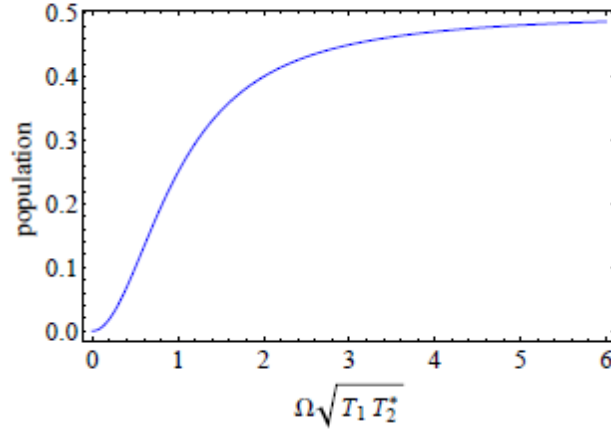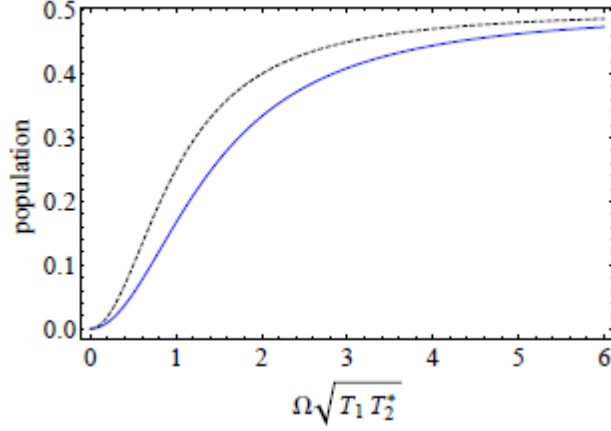
Fig. 12   Steady-state population, see Eqs. 8 and 20

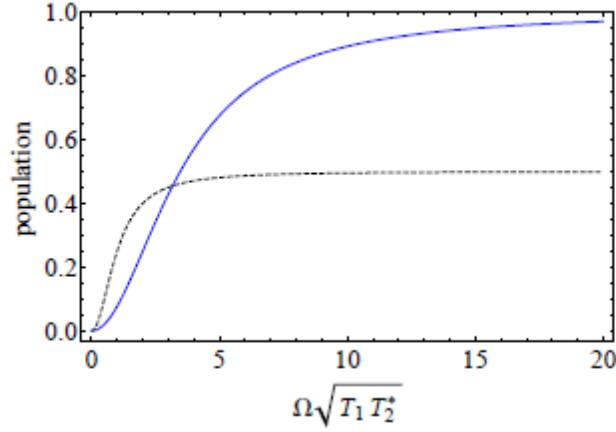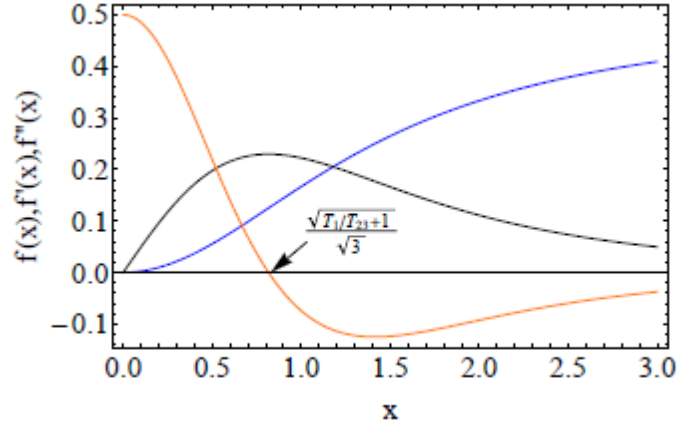**Fig. 13   Useful dependencies to analyze the steady-state population as a function of the field amplitude**

8.   Pulsed Excitation of the 2-Level System

For the 2-level system wave function, $|\Psi(t)\rangle = a_1|1\rangle + a_2|2\rangle$, in the Schrödinger picture the Hamiltonian has the form

$$H = -\frac{\hbar}{2} \begin{pmatrix} 0 & \Omega(t)(e^{i\omega t} + e^{-i\omega t}) \\ \Omega(t)(e^{i\omega t} + e^{-i\omega t}) & -2\omega_2 \end{pmatrix}, \qquad (21)$$

where $\omega_2 = E_2/h$ is the transition frequency (we chose the energy of the ground state $E_1 = 0$), ω is the center frequency of the laser field, $\Omega(t) = E(t)d_{12}/h$ is the time-dependent Rabi frequency, which is determined by the laser field pulse envelope, $E(t)$, and the dipole moment, d_{12}. Using interaction representation and RWA, we obtain the Hamiltonian as

$$\tilde{H} = -\frac{\hbar}{2}\Omega(t) \begin{pmatrix} 0 & e^{i\Delta\omega t} \\ e^{-i\Delta\omega t} & 0 \end{pmatrix}, \tag{22}$$

where detuning $\Delta\omega = \omega - \omega_2$.

To take into account relaxation, we use the master equation for the density matrix $\rho(t)$:

$$\dot{\varrho}(t) = -\frac{i}{\hbar}[\bar{H}\varrho - \varrho\bar{H}]), \tag{23}$$

which allows us to correctly include relaxation terms.

In the Liouvillian form, the final master equation has the form

$$\dot{X}(t) = L(t)X(t), \tag{24}$$

where

$$X(t) = \begin{pmatrix} \varrho_{12}(t) \\ \varrho_{21}(t) \\ \varrho_{11}(t) \\ \varrho_{22}(t) \end{pmatrix}, \tag{25}$$

$$L(t) = \begin{pmatrix} -i\Delta\omega - \frac{1}{T_2^*} & 0 & \frac{-i\Omega(t)}{2} & \frac{i\Omega(t)}{2} \\ 0 & i\Delta\omega - \frac{1}{T_2^*} & \frac{i\Omega(t)}{2} & -\frac{i\Omega(t)}{2} \\ -\frac{i\Omega(t)}{2} & \frac{i\Omega(t)}{2} & 0 & \frac{1}{T_1} \\ \frac{i\Omega(t)}{2} & -\frac{i\Omega(t)}{2} & 0 & -\frac{1}{T_1} \end{pmatrix}. \tag{26}$$

First, let us consider the limiting case of no relaxation and constant Rabi frequency Ω. With the initial condition

$$
X(0) = \begin{pmatrix} \varrho_{12}(0) = 0 \\ \varrho_{21}(0) = 0 \\ \varrho_{11}(0) = 1 \\ \varrho_{22}(0) = 0 \end{pmatrix}
\tag{27}
$$

we obtain

$$
X(t) = \begin{pmatrix} \frac{\Omega\left(\Delta\omega(\cos t\Lambda - 1) - i\sqrt{\Delta\omega^2 + \Omega^2}\sin t\Lambda\right)}{2(\Delta\omega^2 + \Omega^2)} \\ \frac{\Omega\left(\Delta\omega(\cos t\Lambda - 1) + i\sqrt{\Delta\omega^2 + \Omega^2}\sin t\Lambda\right)}{2(\Delta\omega^2 + \Omega^2)} \\ \frac{2\Delta\omega^2 + \Omega^2 + \Omega^2\cos t\Lambda}{2(\Delta\omega^2 + \Omega^2)} \\ \frac{\Omega^2\sin^2\left(\frac{t\Lambda}{2}\right)}{\Delta\omega^2 + \Omega^2} \end{pmatrix}.
\tag{28}
$$

Therefore, in the resonant case, $\Delta\omega = 0$, the population of the excited state is $\varrho_{22}(t)$ $= \sin^2(t\Omega/2)$. Since the PL is proportional to the excited-state population, the integrated PL is

$$
I_{PL}(t) \propto \int_0^t \sin^2\left(t'\Omega/2\right) dt' = \frac{1}{2}\left(t - \frac{\sin\Omega t}{\Omega}\right).
\tag{29}
$$

Figure 14 shows the excited-state population, Eq. 28, and the integrated PL, Eq. 29, as a function of time.
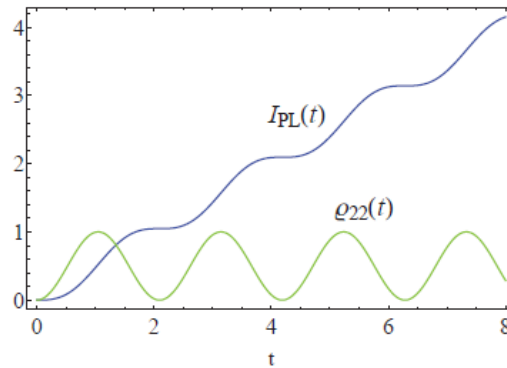
Fig. 14   Integrated PL and the excited-state population vs. time for the limiting case of constant Rabi frequency

To show the relaxation effect and take into account the pulse envelope, we solved the master equation numerically. Figure 15 shows the excited-state population (left panel) and the integrated PL (right panel) as a function of time in the case of pulse excitation with the Rabi frequency envelope shown in Fig. 16.
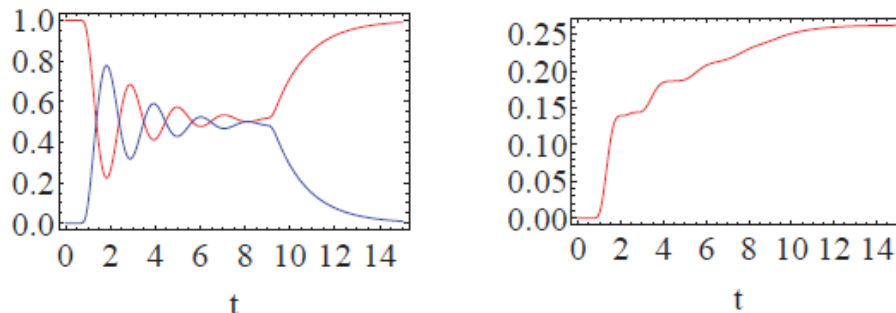
Fig. 15   Integrated PL and the excited-state population vs. time for the pulse excitation
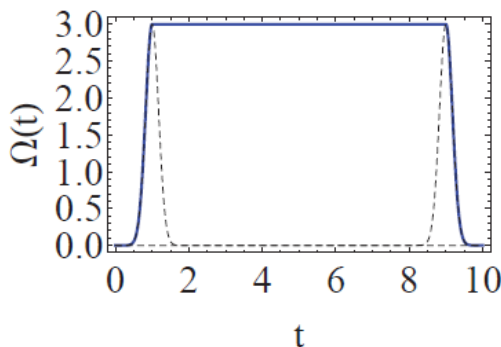
Fig. 16   Rabi frequency vs. time for the pulse excitation

9.   Experimental Work for Nd³⁺:GaN Director's Research Initiative (DRI)

9.1 Growth of Nd³⁺:GaN

Epitaxial GaN:Nd was grown by plasma-assisted molecular beam epitaxy (PA-MBE) in a modular Gen II reactor using liquid gallium, solid Nd, and a nitrogen plasma. A gallium beam equivalent pressure of 1×10^{-7} Torr and a N_2 gas flow of 0.40 sccm was used to grow stoichiometric GaN at 180 nm/h with a step-flow growth morphology resulting in a surface roughness of less than 1 nm. A series of Nd doping calibrations were grown that consisted of 3 layers of GaN:Nd with different Nd source temperatures. The resulting Nd concentrations ranged between 5×10^{17} to 5×10^{18} cm^{-3}. Once calibrated, GaN:Nd films were grown on free-standing GaN substrates with a target Nd concentration of approximately 0.01%, or 4×10^{18} cm^{-3}.

9.2 Continuous-Wave (CW) Steady-State Saturation Photoluminescence (PL) Setup and Experiment

Previous experimental work to characterize the emission and excitation spectrum of Nd^{3+} ions doped in GaN has been used to identify transitions between the $^4F_{3/2}$ excited state to the $^4I_{9/2}$, $^4I_{11/2}$, and $^4I_{13/2}$ multiplets (Fig. 17). For the purpose of quantum memory applications, it was necessary to identify a 2-level system for study within the rich Nd spectrum.
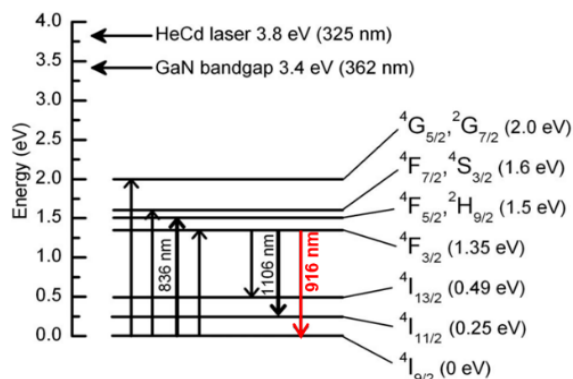
Fig. 17   Simplified energy diagram of the manifolds in the Nd^{3+} ion in GaN. (Reproduced from: Metcalfe G, Redinger E, Shen H, Woodward N, Dieroff V, Wraback M. Crystal-field split levels of Nd3+ ions in GaN measured by luminescence spectroscopy. J Appl Phys. 2009;105:053101., with the permission of AIP Publishing.)
doi: http://dx.doi.org/10.1063/1.3082500

To characterize Nd^{3+}:GaN samples, a near-infrared PL setup was constructed to study the luminescence spectra in an ARL-grown 1.2-µm-thick Nd^{3+}:GaN sample with 0.51% Nd concentration grown by PA-MBE using CW and time-resolved techniques (Fig. 18, left panel). Samples were excited using a 5-W, 532-nm continuous wave (CW) laser to pump a CW Ti:Sapphire laser tunable between 700 and 1000 nm. A CW laser system was used, as opposed to a tunable ultrafast laser system possessing broadband emission, because of the available narrow linewidth (<40 GHz), which enables the individual transitions to be excited selectively. The laser is passed through an optional electro-optic modulator (EOM) or acousto-optic modulator (AOM), which can modulate a square-wave temporal profile on the incident CW laser beam up to 20 MHz. The laser is incident on the sample, which is mounted to a cold finger inside of a closed-cycle helium (He) cryostat capable of providing sample temperatures between 10 K and 300 K. All measurements for this study have been made at the 10-K low-temperature limit. The PL emission is then collected using a pair of lenses to collimate and focus the collected light onto the entrance slit of an 850-mm spectrometer with a 600-g/mm grating and 600-µm-wide entrance and exit slits. After the exit slit of the spectrometer, a rotatable

concave mirror allows for several detection options of the PL signal. To change between multiple detectors with a range of sensitivity and bandwidth, we have fiber coupled one of the outputs so that we can easily use several fiber-based detector options interchangeably. A multimode fiber allows for 70% coupling efficiency from the spectrometer. For the CW PL measurements, both a sensitive, amplified silicon detector and a liquid-nitrogen-cooled Ge detector were used to obtain the PL spectrum using a lock-in amplifier synchronized to the modulation of the excitation laser.
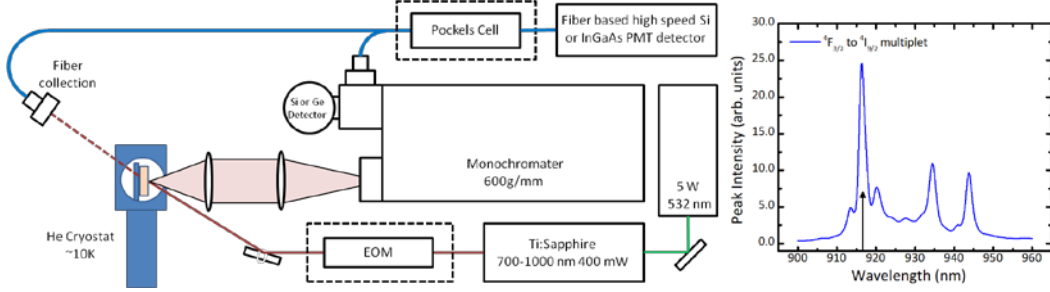

Fig. 18 **Left panel: Experimental setup for CW PL and time-gated PL. Right panel: Emission spectrum from the lower $^4F_{3/2}$ state to the $^4I_{9/2}$ ground multiplet; the arrow indicates the transition between the ground levels of each state at 916.2 nm, which is the strongest.**

The PL spectrum from the lowest $^4F_{3/2}$ multiplet to all $^4I_{9/2}$ multiplets was measured by a free-space variable amplifier Si diode and is shown in the right panel of Fig. 18. To avoid interference from laser scattering, we initially pumped the Nd^{3+}:GaN sample into the $^4F_{5/2}$ state and looked at the emission from the $^4F_{3/2}$ state. The integrated emission from the $^4F_{3/2}$ excited state to the $^4I_{9/2}$ ground state is plotted as a function of the exciting electric field (calculated from the incident laser intensity) in the left panel of Fig. 19, which has been shown capable of determining the dipole moment of the transition from theoretical calculations. The PL emission intensity is fitted assuming a functional form of the saturation dependence of $Y=A(Bx^2)/(1+Bx^2)$. The resulting fit is plotted as the solid blue line in Fig. 19 (left panel), with the 90% confidence bounds of the fit shown in pink. In the right panel of Fig. 19, we have taken the first and second derivative of the PL signal. Modeling demonstrated that the zero crossing ($Y = 0$) of the second derivative of the power-dependent PL occurs at an applied field of $E_0 = 2865$ V/cm when $E_0 d_{12}/\hbar = 1/\sqrt{3T_1 T_2^*}$. Here, T_1 and T_2 are the lifetime of the excited state and the dephasing time, respectively, and d_{12} is the dipole moment for the chosen 2-level system. It is significant to note that the zero crossing of the second derivative is within the excitation range of acquired data and not in the extrapolated portion of the fit.

The strong PL intensity observed in the transitions between the $^4I_{9/2} \leftrightarrow {}^4F_{3/2}$ manifolds suggests that it would make a suitable choice for study. To determine the

optimal transition for study as a 2-level system, it is first important to note that the majority of the population in the ground state will begin in the lowest level of the $^4I_{9/2}$ manifold. Also note that the emission in Fig. 18 from the lowest level within the $^4F_{3/2}$ manifold to the lowest level within the $^4I_{9/2}$ manifold is the most intense. It has been therefore identified that the optimal transition for study as a 2-level system is between the $^4I_{9/2}$ ground state to the lower level in the $^4F_{3/2}$ manifold, which is at 916.2 nm.
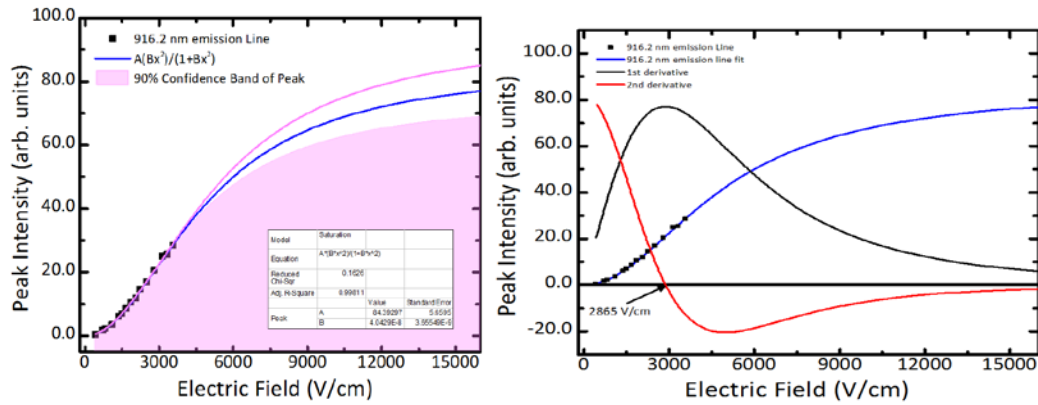
Fig. 19   Left panel: Saturation of the 916.2-nm emission line using 836-nm excitation with increased incident laser electric field strength. Right panel: First and second derivative of the best fit to the saturation data in the left panel. The value at Y = 0 of the second derivative is related to the dipole moment of the transition.

9.3 Characterization of Transition Linewidth

Demonstration of coherence properties requires a high-quality sample with narrow homogeneous and inhomogeneous broadening (linewidth). For this reason, the PL linewidth was characterized for various growth conditions. Figure 20 plots the PL signal recorded for samples with different doping levels and on different substrates: E141 at 0.51% on sapphire, E1524 at 0.05% on free-standing GaN (FS GaN), E1506 at 0.05% on sapphire, and E1507 at 0.1% on sapphire. The PL shows a narrowing of linewidth with both a decrease in Nd doping and with improved crystal quality on FS GaN substrate (E1524). Also, the additional spectra features observed in sample 1507, which are attributed to Nd atom placement on minority sites rather than the majority site, lead to additional broadening. While X-ray analysis has shown no evidence of phase segregation for Nd concentration below 1 atomic %, it is clear from the PL measurements that doping levels at or below 0.05%, grown on native substrates, are necessary to minimize spectral broadening.

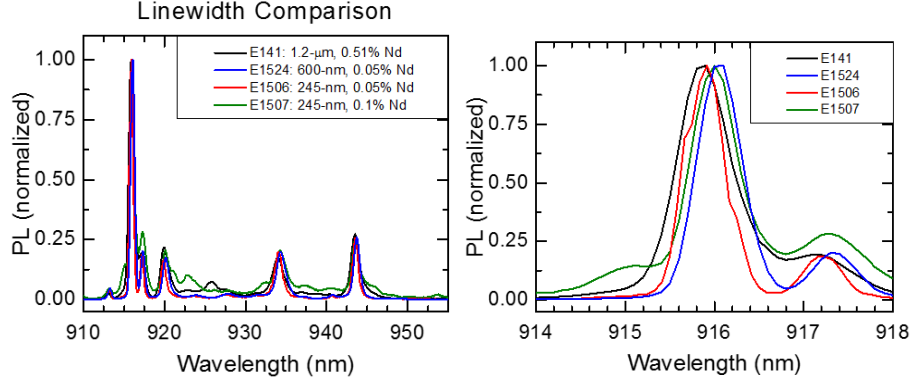**Fig. 20   PL of Nd³⁺:GaN samples with varying doping levels. Right panel: Zoomed-in plot of transition near 916 nm.**

9.4 Time-Gated Photoluminescence (PL) Setup and Experiment for Rabi Oscillations and Photon Echo Measurements

With the spectrum of Nd³⁺:GaN material for study characterized and the transition for the 2-level system identified, the next step involves time-resolved experiments to determine the lifetime of the state as well as the coherence properties of the transition (Rabi frequency, photon echo, etc.). For measurements where the excitation laser and signal detection occur at the same wavelength, it is difficult to separate the 2 signals when interference from scattering of the laser is typically much more intense then the signal of interest. However, it is necessary to make measurements in this way in order to observe transitions within and a 2-level system. We have therefore taken several steps to help eliminate interference from laser light scattering. First, we drilled a hole in the sample mount so that the laser may pass through the sample and ensure that no light is scattered off of the cold finger. Second, polishing the backside of the sample both reduced the overall scattering by the sample and eliminated the scatter of randomly polarized light. Consequently, the scattered laser light maintained its linear polarization and could be reduced further using a linear polarizer at the spectrometer input. Finally, we used the grating in the spectrometer, which diffracts horizontally polarized light more efficiently than vertically polarized light by exciting the sample with vertically polarized light, tuning the polarizer to pass the residual horizontally polarized PL, which detected with higher efficiency because of the polarization dependence of the grating. The combination of these efforts reduced the detected interference from laser scattering by a factor of almost 10^{-4}.

Determining the Rabi frequency informs on the characteristics of the appropriate $\pi/2$ pulse for preparation of the Nd³⁺ ions into the ρ_{11} state and a π pulse to reverse the precession in the *uv*-plane for the observation of a photon echo. For photon echo measurements, sample preparation occurs using a $\pi/2$ pulse followed by a π pulse

at a variable time delay after the $\pi/2$ pulse. Since this is a coherent process, the photon echo is emitted collinearly with the laser excitation. Varying the time delay between the $\pi/2$ and π pulses will result in a change in the amplitude of echo that decays exponentially with the time constant of the decoherence time T_2.

Attempts to observe Rabi oscillations were made by preparing the excitation laser into a square pulse(s) of controllable and variable pulse width, and gating of the signal detection (shown in Fig. 21, left panel). The CW laser is modulated into square pulses of controllable, varying widths between 100 ns and 100 μs, using an AOM. For the initial measurements we used an electro-optic modulator to chop the laser; however, a 2%–5% laser radiation leakage out of the desired pulse window clouded the results. Switching to modulation by the AOM improved the signal-to-noise ratio by more than a factor of 3. A Pockels cell was installed and tested to provide gatable detection. This option to the experimental system provides gated detection with approximately 4-ns rise times and windows between 0 to 1.2 μs. The input to the Pockels cell has been aligned with respect to our fiber coupling to provide the ability to switch between different inputs without the need to further modify the system. A LabVIEW program capable of varying the width of a single pulse, and apply 2 pulses of varying width and spacing, was used.

Ultimately, scattering from the sample still proved too large to observe oscillations in the PL emission at the excitation wavelength. We therefore shifted our detection wavelength to sample decay from the ρ_{11} state to other levels within the $^4I_{9/2}$ manifold to avoid laser interference. This approach was successful in removing effects from scattering; however, only an approximately linear increase of the PL intensity and not oscillations has been observed (Fig. 21, right panel). This could be due to a number of factors, including the relatively wide bandwidth of the excitation laser exciting too wide a bandwidth of the ensemble; the sample temperature being too high, leading to phonon broadening; low detection sensitivity/poor temporal resolution; or short coherence times.
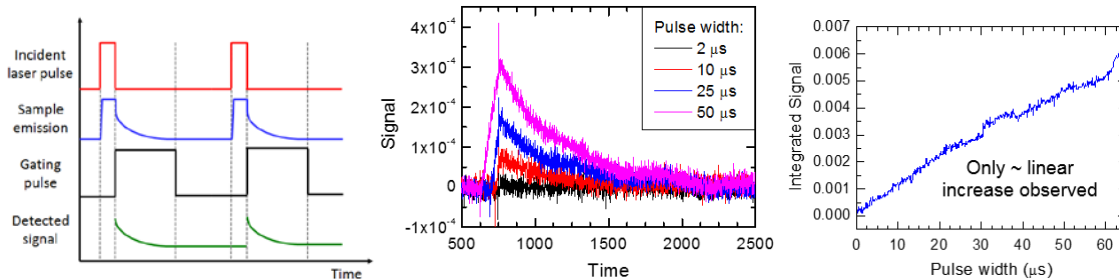

Fig. 21   Left Panel: Timing diagram for the measurement of Rabi oscillations. The gating pulse removed the in-pulse PL signal and laser scattering. Middle Panel: Sample time-resolved PL emission signals for a sampling of pulse widths. Right Panel: Integrated PL signal as a function of gating pulse width shows only a linear increase in signal.

Realizing problems with our laser bandwidth and detection efficiency, we collaborated with Prof Andrei Faraon at the California Institute of Technology. The Caltech group has been working in the area of quantum information of rare-earth doped solids for a number of years and is well equipped to perform coherent spectroscopy of Nd-ion-doped samples. This collaborative work has helped to accelerate the implementation of our research plan and to bring new experimental capabilities and understanding to ARL.

During a visit to Caltech in September 2015, we characterized several in-house-grown samples at their facilities with the intent of performing photon echo and hole-burning measurements, and to try quantum memory experiments based on AFC protocol. Using their frequency-locked, narrow linewidth laser, we were able to observe an approximately 80-pm emission linewidth to the PL signal near 916 nm when a higher manifold was excited, demonstrating a good homogeneous linewidth. The PL decay measurement yielded a result of $T_1 = 150\ \mu s$ (Fig. 22), but we did not observe a photon echo. There are 2 reasons why we were not able to observe a photon echo: 1) the signal is very weak or 2) T_2 is very short. Also, the exponential decay of the photon-echo amplitude at a characteristic time of T_2 implies that a short T_2 will lead to a weak signal. The weak signal for our samples is likely due to the thin-film growth (approximately hundreds of nanometers), which provides orders of magnitude less material (and interaction length) than the approximately 0.5-mm samples the Caltech group typically studies. To address this problem, a waveguide is necessary to increase the interaction length of the interrogation laser. Modeling has demonstrated that it is not possible to grow a coherently strained, quality Nd-doped GaN film of sufficient thickness to confine the laser mode on a layer of material with a satisfactory index mismatch. Two alternative approaches were identified to attain mode confinement. First, the GaN substrate could be removed using a process such as photoelectrochemical (PEC) etching, which would target a sacrificial layer of narrower bandgap grown between the Nd-doped GaN layer and the GaN substrate. Then, waveguide structures could be etched out of the remaining Nd-doped GaN. Second, an (Al)GaAs layer could be grown and etched into a waveguide on top of a high-quality Nd^{3+}:GaN film that would take advantage of the coupling/absorption of the evanescent wave into the Nd^{3+}:GaN. These approaches would require significant effort and development outside of this program.

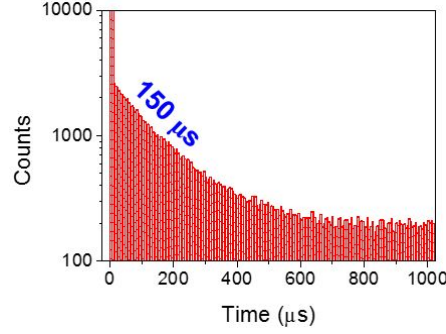**Fig. 22   Measurement of $T_1 = 150$ μs in Nd^{3+}:GaN**

9.5 Characterization of Field-Shifting of Transition Wavelength

In parallel with experiments on the coherence properties of Nd^{3+}:GaN, we also investigated the effect of varying the electric field on the Nd PL spectrum to provide a tunable memory. To vary the applied field, we designed and grew a series of Nd-doped GaN *p-i-n* structures, strain-balanced superlattice (SBSL) structures, and periodic unbalanced (PUB) structures. In the SBSL and PUB structures, the spontaneous polarization discontinuity between AlGaN and GaN layers enable a large range of electric fields to be generated along the c-direction. Modeling of the built-in electric fields was performed using a self-consistent drift-diffusion model. In the SBSL design, higher fields were targeted using periodic structures grown with alternating layers of GaN and $Al_xGa_{1-x}N$ with equal thicknesses, strain-balanced to a template layer of $Al_{x/2}Ga_{1-x/2}N$. The PUB structures were necessary to target fields below approximately 500 kV/cm because of the large thicknesses required in the SBSLs for low-field intensities, which would likely lead to misfit defect formation and increase the inhomogeneous broadening of the Nd^{3+} ion transitions. This was accomplished using thin, periodic, low-Al mole fraction AlGaN-strained layers grown pseudomorphically to a free-standing GaN substrate to induce a field in the alternating Nd-doped GaN layers.

Figure 23 summarizes the modeled electric field ranges possible for different AlGaN/GaN SBSL and PUB designs. We have completed the layer structure designs for both the SBSL and the PUB structures, and we have grown structures with calculated electric field strengths ranging from 274 kV/cm to 4.5 MV/cm by growing 2 series: SBSL structures using $Al_{0.8}Ga_{0.2}N$ barriers on an $Al_{0.4}Ga_{0.6}N$ template layer (orange line) and the PUB structures with $Al_{0.2}Ga_{0.8}N$ barriers on a FS GaN substrate (green line). SIMS measurements were performed to validate that Nd incorporation occurred in the desired layer. Figure 24 plots the SIMS measurement on the 60-nm-thick well/barrier SBSL sample that demonstrates that Nd incorporation is present in the GaN layers (within the resolution of the measurement).
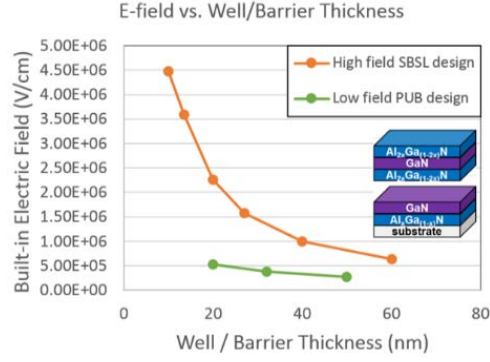
Fig. 23 Electric field vs. GaN well/ $Al_xGa_{(1-x)}N$ barrier thickness for strain-balanced superlattice (SBSL) structures with GaN wells/ $Al_{0.8}Ga_{0.2}N$ barriers (orange line) and periodic unbalanced (PUB) structures with GaN wells and $Al_{0.2}Ga_{0.8}N$ barriers (green line)
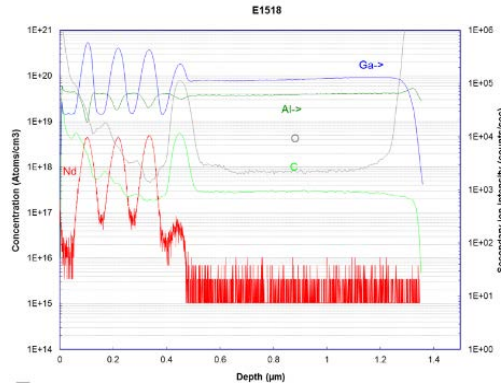

Fig. 24 SIMS measurement on the 60-nm-thick well/barrier SBSL sample

Figure 25 plots the PL spectra of the series of high-field SBSL samples (with designed electric fields of 640 kV/cm, 1.0 MV/cm, 2.3 MV/cm, and 4.5 MV/cm) and an approximately zero-field 600-nm bulk Nd-doped GaN sample and a high-field (~4.5 MV/cm). PL spectra were acquired using a tunable pulsed Ti:Sapphire laser with wide spectral bandwidth tuned to excite transitions from the $4I_{9/2}$ ground state to the $4F_{5/2}$ manifold near 836 nm at 10 K (to ensure that most of the population in the ground state would begin in the lowest level of the $4I_{9/2}$ manifold). PL from the lower-energy $4F_{3/2}$ manifold to the $4I_{9/2}$ manifold was detected using a Fourier-transform infrared spectrometer (FTIR) to separate transitions and capture the entire spectrum at once. This broadband approach was employed to mitigate the difficulty that results from excitation and emission linewidths shifting spectrally. A nearly identical shift of greater than 1.1 nm is observed in the PL spectra for each sample, demonstrating the ability to tune the Nd transition with field. However, the magnitude of the shift observed (>300 GHz) is more than an order of magnitude larger than expected for a Stark shift at these built-in electric fields.
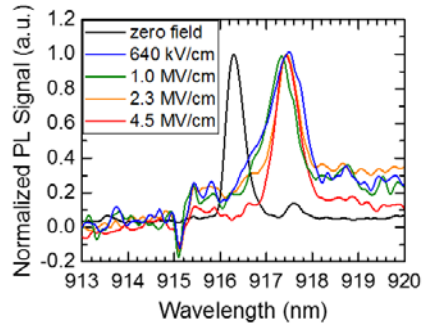
Fig. 25 Nd^{3+}:GaN PL spectra of an approximately zero-field bulk sample and high-field SBSL samples (expected electric field strength given in legend)

We therefore began a collaboration with Profs David Smith and Martha McCartney at Arizona State University to perform electron holography on our samples to provide a direct measurement of electric field. Results from that study were both informative and perplexing. Transmission electron microscopy (TEM) images are shown in Fig. 26 for sample E1521; the 40-nm-thick well/barrier SBSL sample is expected to possess a built-in electric field of approximately 1 MV/cm. It is apparent that the layered structure is compromised with irregular interfaces and facets that are likely due to propogation of defects from the substrate layer (see upward "lines" in the base of Fig. 26, left panel, that seem to lead to sharp structures farther up in the sample). The propogation of these defects likely expose different crystal planes (rather than the desired c-plane), which posses differing growth rates and lead to the observed structuring of the periodic sample.

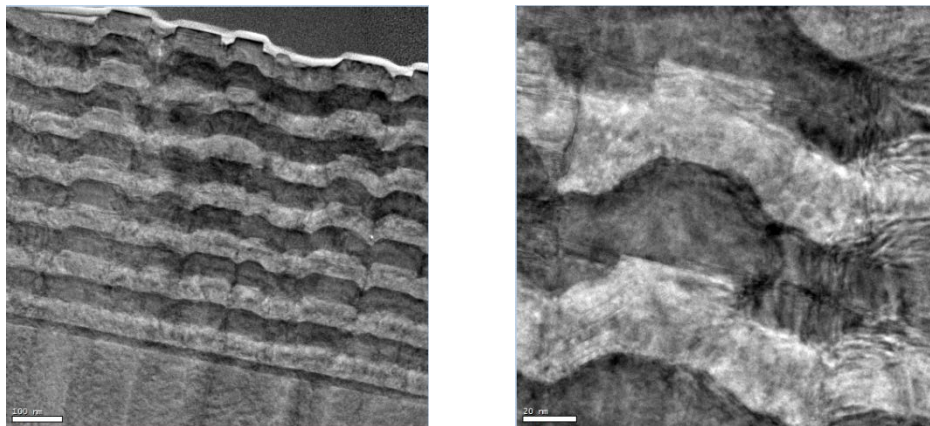
Fig. 26 TEM images of sample 1521, the 40-nm-thick well/barrier SBSL sample, with a 100-nm scale bar (left panel) and a 20-nm scale bar (right panel).

The TEM images of sample 1521 were processed using an electron holography approach described in McCartney and Smith.[14] Briefly, the technique images the phase shift of an electron beam that passes through a sample with one that passes

29

through vacuum. A sample phase image for sample E1521 is shown in Fig. 26 (left panel). The brighter areas are GaN, where the built-in electric field, E, is indicated, and the darker areas are AlGaN. The area within the outlined area in Fig. 26 (left panel) is plotted as a line profile of phase (in radians) in Fig. 26 (right panel). The formula for converting the phase image to electrostatic potential is

$$\Delta\varphi(x,y) = \int_0^t C_E V(x,y,z)dz \sim C_E V(x,y)t(x,y) , \qquad (30)$$

where $\Delta\varphi$ is the phase difference (from vacuum, for example, or from one side of the layer to the other), C_E is a constant that depends on accelerating energy, and t is the thickness. Equation 30 assumes that the potential is constant throughout the thickness, which ignores the surface effects in the thin film, but since the sample is approximately tens to hundreds of nanometers thick, "bulk" effects can be assumed to dominate. Another important approximation assumes that there are no other phase-shifting mechanisms. Estimates of the built-in electric field throughout the sample (beyond the shown images area in Fig. 27) yield electric fields in the AlGaN layers on the order of 0.10 MV/cm, and the field in the GaN layers to be in the 0.10–0.25 MV/cm range. Each estimate is considerably lower than what is modeled for this structure, where an approximately 1-MV/cm electric field magnitude is expected in the GaN layer.
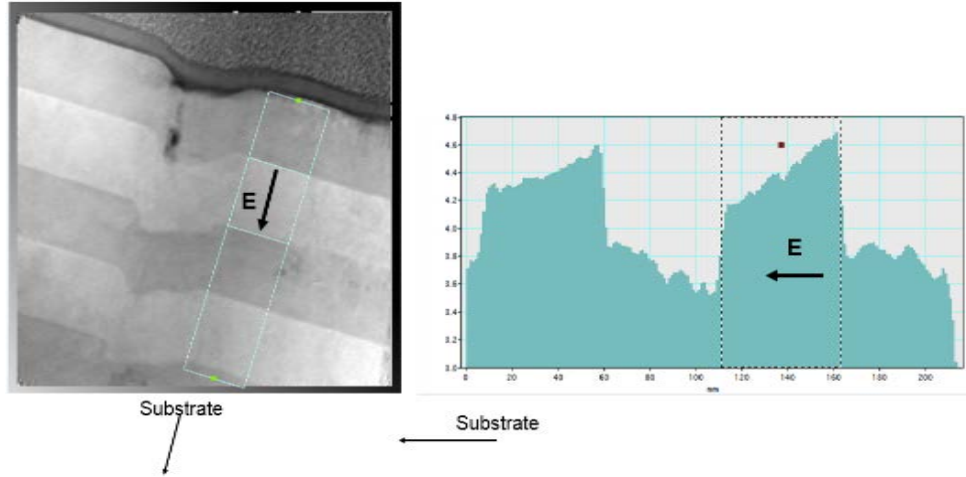
Fig. 27 Electron holography phase image (left panel) with area for line profile (right panel) outlined. Brighter areas are GaN, and darker areas are AlGaN.

The lower-than-expected estimate further complicates the larger-than-expected spectral shift of the PL wavelength for the identified transition. The clear implication is that the spectral shift is due to some other effect than the built-in electric field due to the heterostructure. An initial theory that the overall crystal field—due to the on-average crystal structure of $Al_{0.4}Ga_{0.6}N$, coherently strained to

a base layer of $Al_{0.4}Ga_{0.6}N$—is dominating the transition wavelength has been eliminated since the transition in the binary AlN shifts to shorter, not longer, wavelengths than the Nd^{3+}:GaN transition. A remaining theory suggests the mechanism that shifts the PL wavelength is due to the complex strain state of the highly defective sample, which results in space charge at the defect locations. Further investigation of this phenomena will focus on samples grown on high-quality substrates, such as the set of low-field PUB samples and *p-i-n* structures that can be biased to determine the functional dependence of the shifted Nd transition on applied field.

10. Conclusion

In this DRI program, we investigated the potential of a cryogenically-cooled REIC, Nd^{3+}:GaN, for use as tunable solid state quantum memory. Theoretically, we developed a quantum description of 2- and 3-level systems and of the 2- and 3-pulse photon echo effect, and estimated the effect of an applied electric field for control of collective coherences using the linear Stark effect. Experimentally, PL measurements were used to study the energy level structure of the Nd ions embedded into the crystal lattice of GaN. The power dependence of the PL emission intensity was used to determine a relation between key parameters, while the decay rate of the PL emission yielded an excited state lifetime of $T_1 \approx 150$ µs. SBSL structures with high built-in fields demonstrated the ability to shift the Nd transition wavelength, however results were dominated by sample defects. Additional work is required to determine the dependence of the Stark shift on electric field and to measure the coherence times in Nd^{3+}:GaN waveguide structures.

11. References

1. Tittle W, Afzelius M, Chaneliere T, Cone RL, Kröll S, Moiseev SA, Sellars M. Photon-echo quantum memory in solid state systems. Laser & Photon Re. 2010;4:244–267.

2. Hammerer K, Sorensen A, Polzik E. Quantum interface between light and atomic ensembles. Rev Mod Phys. 2010;82:1041.

3. Ruggiero J, LeGouet JL, Simon C, Chaneliere T. Why the two-pulse photon echo is not a good quantum memory protocol. Phys Rev A. 2009;79:053851.

4. Moiseev SA, Kröll S. Complete reconstruction of the quantum state of a single-photon wave packet absorbed by a Doppler-broadened transition. Phys Rev Lett. 2001;87:173601. Kraus B, Tittel W, Gisin N, Nilsson M, Kröll S, Cirac JI. Quantum memory for nonstationary light fields based on controlled reversible inhomogeneous broadening. Phys Rev A. 2006;73:020302.

5. Afzelius M, Simon C, Riedmatten H, Gisin N. Multimode quantum memory based on atomic frequency combs. Phys Rev A. 2009;79:052329.

6. Ruggiero J, LeGouet JL, Simon C, Chaneliere T. Why the two-pulse photon echo is not a good quantum memory protocol. Phys Rev A. 2009;79:053851.

7. Berman PR, Malinovsky VS. Principles of laser spectroscopy and quantum optics. Princeton (NJ): Princeton University Press; 2011.

8. Elyutin SO, Zakharov SM, Manykin EA. Sov Phys JETP. 1979;49:421; Mossberg TW. Time-domain frequency-selective optical data storage. Opt Lett. 1982;7:77.

9. Simon C, de Riedmatten H, Afzelius M, Sangouard N, Zbinden H, Gisin N. Quantum repeaters with photon pair sources and multi-mode memories. Phys Rev Lett. 2007;98:190503.

10. Metcalfe G, Redinger E, Shen H, Woodward N, Dieroff V, Wraback M. Crystal-field split levels of Nd3+ ions in GaN measured by luminescence spectroscopy. J Appl Phys. 2009;105:053101.

11. Liu G, Jacquier B, Editors. Spectroscopic properties of rare earths in optical materials; Springer Series in Materials Science. New York (NY): Springer; 2005.

12. Macfarlane RM. Optical Stark spectroscopy of solids. J Luminescence. 2007;125:156.

13. Readinger ED, Metcalfe GD, Shen H, Wraback M. GaN doped with neodymium by plasma-assisted molecular beam epitaxy. App Phys Lett. 2008;92:061108.

14. McCartney MR, Smith DJ. Electron holography: phase imaging with nanometer resolution. Annual Review of Materials Research. 2007;37:729–767.

List of Symbols, Acronyms, and Abbreviations

3-D	3-dimensional
AFC	atomic frequency comb
AlN	aluminum nitride
AOM	acousto-optic modulator
ARL	US Army Research Laboratory
at%	atomic-percent
CRIB	controlled reversible inhomogeneous broadening
CW	continuous wave
DC	direct current
DRI	Director's Research Initiative
FS GaN	free-standing gallium nitride
FTIR	Fourier-transform infrared spectrometer
GaN	gallium nitride
He	helium
MBE	molecular beam epitaxy
Nd	neodymium
OPA	optical parametric amplifier
PA-MBE	plasma-assisted molecular beam epitaxy
PEC	photoelectrochemical
PL	photoluminescence
PLE	photoluminescence excitation
PUB	periodic unbalanced
REIC	rare-earth-ion-doped crystal
RF	radio frequency
RS	Russell-Saunders

RWA   rotating-wave approximation

SBSL   strain-balanced superlattice

SIMS   secondary ion mass spectrometry

TEM   transmission electron microscopy

XRD   X-ray diffraction

1   DEFENSE TECH INFO CTR
(PDF) DTIC OCA

       2   US ARMY RSRCH LAB
(PDF) IMAL HRA MAIL & RECORDS MGMT
            RDRL CIO L TECHL LIB

       1   GOVT PRNTG OFC
(PDF) A MALHOTRA

       5   US ARMY RSRCH LAB
(PDF) RDRL SEE M
             G D METCALFE
             R ENCK
            RDRL SEE I
             B CONNELLY
             S RUDIN
             V MALINOVSKY